Probing transverse magnetic anisotropy by electronic transport through a single-molecule magnet

M. Misiorny,[1,2,*] E. Burzurí,[3,†] R. Gaudenzi,[3] K. Park,[4] M. Leijnse,[5] M. R. Wegewijs,[1,6] J. Paaske,[7] A. Cornia,[8] and H. S. J. van der Zant[3]

[1]*Peter Grünberg Institut & JARA, Forschungszentrum Jülich, 52425 Jülich, Germany*
[2]*Faculty of Physics, Adam Mickiewicz University, 61-614 Poznań, Poland*
[3]*Kavli Institute of Nanoscience, Delft University of Technology, 2600 GA, Delft, The Netherlands*
[4]*Department of Physics, Virginia Tech, Blacksburg, Virginia 24061, USA*
[5]*Solid State Physics and Nanometer Structure Consortium (nmC@LU), Lund University, Box 118, S-22100 Lund, Sweden*
[6]*Institute for Theory of Statistical Physics, RWTH Aachen, 52056 Aachen, Germany*
[7]*Center for Quantum Devices, Niels Bohr Institute, University of Copenhagen, 2100 Copenhagen, Denmark*
[8]*Department of Chemical and Geological Sciences and INSTM, University of Modena and Reggio Emilia, via Giuseppe Campi 183, I-41125 Modena, Italy*

(Received 18 July 2014; revised manuscript received 16 January 2015; published 30 January 2015)

By means of electronic transport, we study the transverse magnetic anisotropy of an individual Fe_4 single-molecule magnet (SMM) embedded in a three-terminal junction. In particular, we determine *in situ* the transverse anisotropy of the molecule from the pronounced intensity modulations of the linear conductance, which are observed as a function of applied magnetic field. The proposed technique works at temperatures exceeding the energy scale of the tunnel splittings of the SMM. We deduce that the transverse anisotropy for a single Fe_4 molecule captured in a junction is substantially larger than the bulk value.

DOI: 10.1103/PhysRevB.91.035442 PACS number(s): 75.50.Xx, 75.30.Gw, 73.63.−b, 75.76.+j

I. INTRODUCTION

Single-molecule magnets (SMMs) [1] have been proposed as candidates for applications in molecular spintronics [2–7]. Especially enticing is the prospect of using an individual SMM as a base component of a spintronic circuit which would be capable of storing [8] or processing [7,9–11] classical and quantum information. In general, the essential prerequisite for this is a magnetic bistability which in SMMs stems from a large molecular spin and a strong *easy-axis* magnetic anisotropy, given by a parameter D. This tends to fix the spin along an axis determined by the molecular structure, without favoring any specific direction along this axis. In consequence, an energy barrier $\sim DS^2$ protects the spin of the molecule against reversal between the two opposite, energetically degenerate orientations. From this point of view, detection of the additional *transverse* magnetic anisotropy, characterized by the parameter $E > 0$ in the Hamiltonian $\hat{\mathcal{H}} = -D\hat{S}_z^2 + E(\hat{S}_x^2 - \hat{S}_y^2)$, is crucially important. Such transverse anisotropy can impair the bistability by opening under-barrier quantum tunneling channels for spin reversal [1,12,13]. These quantum tunneling processes are also of fundamental interest since the spin-dynamics displays pronounced geometric or Berry-phase effects [14–19].

Hitherto, most techniques aiming to extract the transverse anisotropy parameter E are based on the detection of the tunnel splittings it induces, which display a characteristic magnetic field dependence [1,12]. The major challenge for all such approaches is that these splittings are complicated functions of E, and even more, the splitting for high-spin states and low magnetic fields are smaller than the parameter E itself by several orders of magnitude. Using Landau-Zener spectroscopy the tunnel splittings have been accurately determined in bulk Fe_8 by measuring their pronounced Berry-phase oscillations [14]. Also in bulk crystals and solutions of SMMs the parameter E has been established by different methods, such as high-frequency electron paramagnetic resonance [20,21] and inelastic neutron scattering [22]. These methods, however, probe large assemblies of molecules and thus are not designed for investigating the magnetic properties of an individual SMM. As a result, little is known about the transverse anisotropy of individual SMMs in spintronic devices.

In this paper we propose an approach for extracting the parameter E of a single molecule by employing electronic transport measurements. We study a Fe_4 SMM captured in a gateable junction (for details see Appendix A)—a geometry close to envisaged device structures—which is a unique tool for addressing the spin in different redox states of a molecule [5]. We show that, as a consequence of the mixing of the spin eigenstates of the SMM, the transverse anisotropy significantly manifests itself in transport. In particular, we predict and experimentally observe characteristic variations of the Coulomb peak *amplitude* with the magnetic field from which the parameter E can be estimated. Importantly, the method proposed here works at temperatures and electron tunnel broadenings Γ exceeding E by many orders of magnitude, while E, in its turn, much exceeds the tunnel splittings.

II. THREE-TERMINAL SMM JUNCTIONS

A scheme of a three-terminal SMM junction is shown in Fig. 1(a). An SMM bridges the source and drain gold electrodes. An underlying aluminum electrode separated by a few nanometers of aluminum oxide allows for electrical gating of the molecule and, thus, accessing different redox states; see also Appendix A2. The chip containing the junctions is mounted on a piezo-driven rotator that enables to change *in situ* the orientation between the external

*misiorny@amu.edu.pl
†E.BurzuriLinares@tudelft.nl

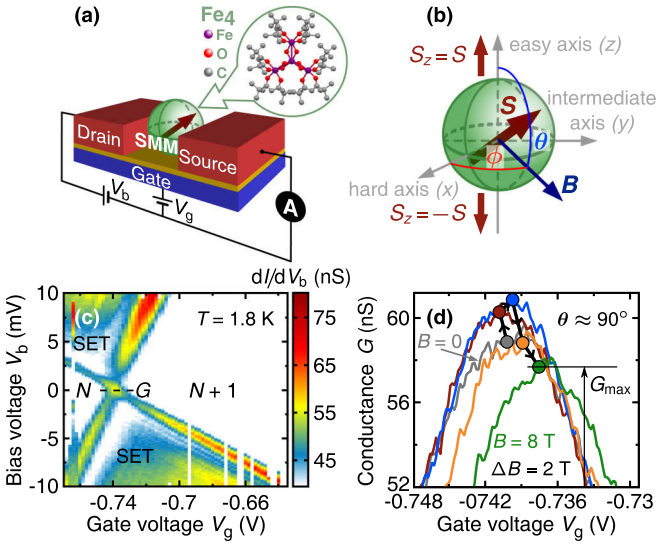

FIG. 1. (Color online) (a) Schematic depiction of a molecular three-terminal transistor with a single Fe_4 SMM bridging the junction. (b) Spatial orientation of an external magnetic field with respect to the principal axes set by the magnetic anisotropy of an SMM. (c) Differential-conductance map, dI/dV_b, measured as a function of gate V_g and bias V_b voltages showing two charge states N (neutral) and $N+1$ (charged) for sample A. (d) Representative Coulomb peaks [corresponding to linear conductance $G \equiv dI/dV_b|_{V_b=0}$, e.g., marked by dashed line in (c)] measured at different values of the external magnetic field B. The bold arrowed lines and color dots serve as a guide for eyes to indicate the nonmonotonic change in the Coulomb peak height.

magnetic field $\boldsymbol{B}$ and the magnetic anisotropy axes of the molecule, which is characterized by angles θ and ϕ as illustrated in Fig. 1(b). All the measurements are performed at $T = 1.8$ K.

The differential conductance plotted in Fig. 1(c) shows the standard signatures of sequential electron tunneling (SET) through a molecule with two competing charge states tuned by a gate voltage [23]. Strong high-conductance resonance lines separate adjacent charge-stable Coulomb blockade regions, labeled N and $N+1$, from the SET regions where transport is possible. Importantly, several fingerprint features of the stable Fe_4 SMM can be identified: (i) high charging energies expected for an individual molecule; (ii) a strong SET excitation at approximately 4.8 meV [5], specific to Fe_4 as it corresponds to the predicted transition energy between the ground ($S_N = 5$) and the first-excited ($S_N = 4$) spin multiplets for the neutral molecule [20]; (iii) a non-linear shift of the degeneracy peak in the presence of magnetic field as described by gate-voltage spectroscopy (for details see Ref. [24] and Appendix A3). Moreover, depending on the strength of tunnel coupling Γ, split Kondo zero-bias anomalies in Coulomb blockade regimes of *subsequent* charge states can be observed, which show the zero-field splitting (ZFS) at the values expected for the Fe_4 SMM [5,25]. These features also indicate that the molecule is in an intermediate coupling regime with the electrodes, with its upper limit estimated to be $\Gamma = 1.6$ meV, obtained from the full width at half maximum of the crossing (degeneracy) point of the Coulomb edges at zero bias, the Coulomb peak; for further discussion see Appendix A3.

III. GATE-VOLTAGE "POSITION" SPECTROSCOPY

In a magnetic field the position of the Coulomb peak (CP) depends both on the *magnitude* and the *orientation* of an external magnetic field $\boldsymbol{B}$ [24]. In short, the CP marks the transition between the ground states of two spin multiplets, with spin values S_N and S_{N+1}, for the two neighboring charge states. The energy difference between these states is then a function of $\boldsymbol{B}$, and in particular, it translates into a shift of the linear response degeneracy point in V_g, as shown in Fig. 1(d). From such a shift one can infer that the ground spin-multiplets of the two charge states evolve differently in the applied field; therefore, the shift provides information about the magnetic properties of the system. For example, in simple quantum dots the shift corresponds just to the *linear* Zeeman effect which is *isotropic* [26]. On the other hand, for magnetically anisotropic molecules, like the SMMs discussed here, not only does the CP shift depend on the relative sample-field orientation, allowing us to extract the value of the angle θ, but it also provides information about the uniaxial magnetic anisotropy (D) [24]. However, the gate-voltage position of the peak, determined by the low-energy spectrum, is insensitive to the small tunnel splitting corrections induced by the transverse magnetic anisotropy. Below we show that information about the transverse magnetic anisotropy (E) can instead be inferred from a nonmonotonic dependence of the peak *amplitude* G_{max}, such as in Fig. 1(d), which relies on transition probabilities between different spin states. We have measured around 200 junctions, of which 17 showed clear molecular signatures. From those, 9 samples displayed a clear CP suitable to perform gate spectroscopy and a magnetic field modulation of G_{max}. Further discussion of statistics together with differential-conductance maps for several devices are presented in Appendix A4.

In Fig. 2(a) the amplitude G_{max} of the CP, normalized to its value at $B = 0$, is plotted as a function of B for two different samples. For both samples, the gate-voltage analysis of the peak position allows us to conclude that the magnetic field lies in the hard plane ($\theta \approx 90°$); see Appendix A3. Interestingly, $G_{max}(B)$ for the two samples exhibits a significantly different behavior. If only uniaxial magnetic anisotropy was present ($E = 0$), the transport properties of the molecule would be left unaffected upon rotation of the field in the hard plane. On the contrary, for $E \neq 0$ this rotational symmetry is broken. The dissimilar behavior of the amplitude G_{max} as observed in Fig. 2(a) is therefore attributed to different values of the angle ϕ in the presence of a nonzero E. Similar curve shapes have been observed in additional samples, as shown in Fig. 9. Although the values of E for bulk samples/monolayers of SMMs are typically small (for Fe_4 $E/D \lesssim 0.07$) [21,27], the linear conductance through a molecule appears to be measurably influenced by it. A similar change in the field-evolution of G_{max} is also observed in a single sample C, shown in Fig. 2(b), by rotating the sample holder relative to the magnetic field.

IV. THEORY AND DISCUSSION

In order to understand how the transverse magnetic anisotropy could qualitatively affect the linear conductance through an SMM (i.e., the CP amplitude), while hardly influ-

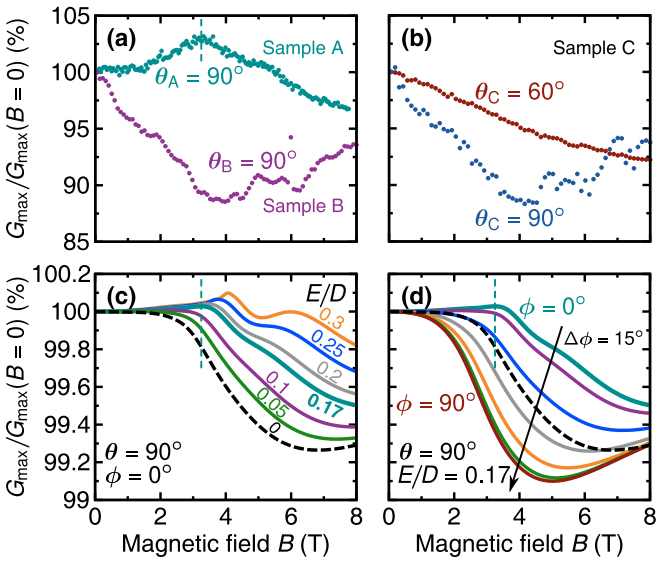

FIG. 2. (Color online) Signatures of transverse magnetic anisotropy in electronic transport at $T = 1.8$ K. (a) Dependence of the Coulomb peak (CP) height G_{max} [i.e., the maximal value of G; cf. Fig. 1(d) on magnetic field B shown for two different samples where the orientation of the magnetic field lies in the hard plane ($\theta = 90°$). (b) Analogous to (a) for a single sample, except that now θ is varied and ϕ is unknown. Note that the evolution of the CP position in magnetic field, and not G_{max}, was previously analyzed in Ref. [24] for samples A and C. (Bottom panels) Theoretical predictions for evolution of the CP height with magnetic field B kept in the hard plane (c) for indicated values of E/D and $\phi = 0°$, whereas in (d) for several angles ϕ and the fixed value of E/D estimated from (a). Bold dashed lines represent the case of $E/D = 0$ for $\phi = 0°$ (c) and $\phi = 90°$ (d). Notice that the shape of G_{max} for $E/D = 0$ is independent of ϕ due to the rotational symmetry around the molecule's easy axis.

encing its gate-voltage position, we use a minimal molecular quantum-dot model based on two giant-spin Hamiltonians [1],

$$\hat{\mathcal{H}}_{SMM} = \sum_{n=N,N+1} [\hat{\mathcal{H}}_n + \hat{\mathcal{H}}_n^Z], \quad (1)$$

one for each charge state. Here $\hat{\mathcal{H}}_n$ accounts for the magnetic anisotropy of the SMM in the nth charge state,

$$\hat{\mathcal{H}}_n = -D_n(\hat{S}_n^z)^2 + E_n[(\hat{S}_n^x)^2 - (\hat{S}_n^y)^2], \quad (2)$$

with the first (second) term representing the uniaxial (transverse) magnetic anisotropy, and $\hat{\mathcal{H}}_n^Z = g\mu_b \boldsymbol{B} \cdot \hat{\boldsymbol{S}}_n$ is the Zeeman term ($g \approx 2$). We combine this with a master equation description of the SET transport to nonmagnetic electrodes with tunnel coupling Γ [16,28,29]. The essential steps of this approach are provided in Appendix B3. The appearance of a clear CP in the experiment restricts $S_{N+1} = S_N \pm 1/2$ (otherwise spin blockade would be seen) [5]. For the Fe_4 SMM we can estimate $S_N = 5$ and $D_N \equiv D \approx 56$ μeV for the neutral state, whereas from the CP position dependence we obtain $S_{N+1} = 9/2$ and fix $D_{N+1} \approx 1.2D = 68$ μeV with approximately collinear easy axes for both charge states, all in agreement with previous measurements [24]; see also Appendix A3. We assume that upon charging only the overall energy scale of the magnetic anisotropy changes, i.e., $E_N/D_N \approx E_{N+1}/D_{N+1}$, leaving just a single parameter $E_N = E$ for the transverse anisotropy.

In Fig. 2(c) we plot the calculated CP amplitude G_{max} for $\theta = 90°$ and $\phi = 0°$ as a function of the applied field B. Surprisingly, the calculations reveal that a nonzero value of E significantly influences the current through the molecule. By adjusting the parameter E/D, qualitative agreement with the measured amplitude variation is obtained for sample A when $E/D \approx 0.15$–0.2. The dissimilar behavior of G_{max} between samples A and B is then qualitatively reproduced when assuming strongly differing values of the angle ϕ as shown in Fig. 2(d). From the shape of the curves we estimate the value of ϕ to be $\phi_A \approx 0°$ for sample A and $\phi_B \approx 90°$ for sample B. Note that the minimum of G_{max} for $\phi = 90°$ appears in Fig. 2(d) at a somewhat larger B field value than for sample B, which signifies larger E/D; cf. Figs. 13–15. Therefore, combining the information from Figs. 2(c) and 2(d), the CP amplitude could be used to estimate the values of E and ϕ. The obtained rough estimate $E/D \approx 0.17$ is larger than the values reported for bulk samples [27], as also suggested by x-ray magnetic circular dichroism (XMCD) experiments on Fe_4 monolayers deposited on gold [21].

To gain deeper insight into the mechanism leading to a modulation of G_{max}, we analyze in Fig. 3(a) how the calculated B traces of the CP amplitude evolve with temperature. The appearance of a maximum at around $B = 3.25$ T (marked by the vertical dashed line) and its enhancement with increasing temperature suggests that this feature is built up from contributions of many excited states of the SMM. This is indeed confirmed by inspection of the evolution of the occupation probabilities shown in Fig. 3(b) for the experimental temperature $T = 1.8$ K. To obtain this figure we first find the eigenstates of $\hat{\mathcal{H}}_n$, given by Eq. (2). For $n = N, N+1$ we obtain two sets of eigenspectra, $\{\varepsilon_N^{k'}\}$ and $\{\varepsilon_{N+1}^{k}\}$. Here k' and k label the states in order of increasing energy, starting from $k' = 0$ ($k = 0$) for the neutral (charged) *ground* state. Using these energies and states, we calculate the probabilities from the master equation. One should note that the energies [see Fig. 4(b)] and occupation probabilities of corresponding states ($k = k'$) for different charge are very similar. From Fig. 3(b), however, it is not clear which of the maxima of the probabilities is responsible for the maximum of the $G_{max}(B)$ curves, indicated by the vertical dashed line.

Instead, to understand the $G_{max}(B)$ dependence in Fig. 3(a), one has to consider the transition energies $\varepsilon_{N+1}^{k} - \varepsilon_N^{k'}$ between levels of different charge states. This is demonstrated in Fig. 3(c) (see also Fig. 4), where the horizontal dashed lines represent the available thermal energy. The transition energies fall into three generic groups: (i) low-energy transitions ($k = k'$, green lines); (ii) transitions of low energy for small B but high energy for large B ($k,k' = 0,1$ or $k,k' = 2,3$, orange lines); (iii) high-energy transitions (remaining k and k' pairs, blue lines). Importantly, the temperatures used in Fig. 3(a) lie just below the group of transition-energy curves exhibiting a minimum at finite magnetic fields roughly between 2 and 4 T [blue curves in Fig. 3(c). As the magnetic field is augmented from zero, these curves thus initially approach the thermal energy (horizontal dashed lines) before moving away at higher fields towards their high-field asymptotes. This

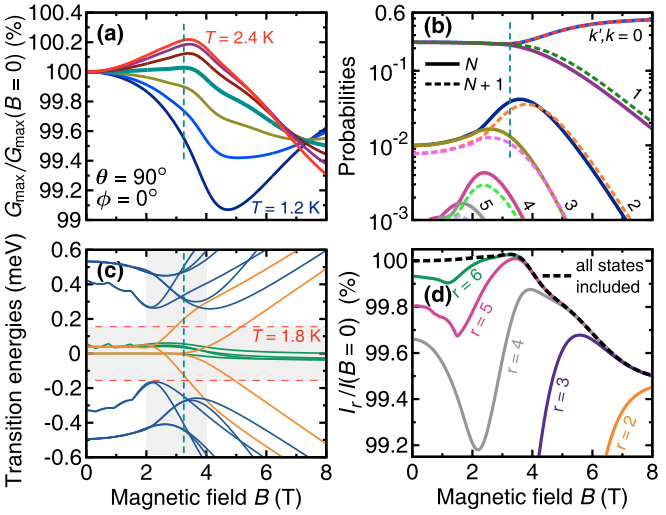

FIG. 3. (Color online) Theoretical analysis of transport for fixed $D = 56$ μeV and $E/D = 0.17$ and $\boldsymbol{B}$ along the hard axis ($\theta = 90^\circ$ and $\phi = 0^\circ$). (a) Conductance $G_{\max}(B)$ traces for various temperatures over the range 1.2 K–2.4 K at intervals of 0.2 K. (b) Occupation probabilities for several lowest-energy states in the spin multiplets for N and $N+1$ at $T = 1.8$ K. Here k' (k) labels the states in order of increasing energy for N ($N+1$), with $k' = 0$ ($k = 0$) denoting the ground state. (c) Relevant transition energies $\varepsilon^k_{N+1} - \varepsilon^{k'}_N$ for $k,k' \leq 4$ determining the SET processes at the Coulomb resonance (note that $\varepsilon^0_{N+1} = \varepsilon^0_N$ is restored for each B by tuning V_g). Different colors of lines are used to distinguish groups of transitions with respect to possible combinations of indices k and k' (see the main text). For the association of these lines with specific transitions as well as the energies of individual levels see Fig. 4. (d) Evolution of the current vs magnetic field at $T = 1.8$ K calculated by including a restricted number of states per spin multiplet up to r, where $r = k'_{\max} + 1 = k_{\max} + 1$, showing that for small r significant deviations are found compared to the calculation involving all the states (dashed line), used in all other plots. For a precise definition of the current I_r see Appendix B3.

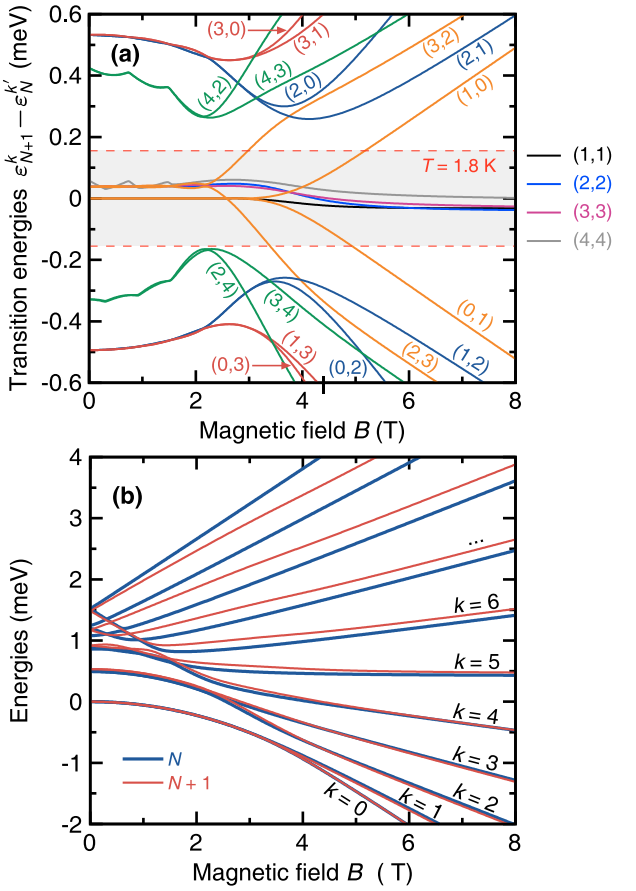

FIG. 4. (Color online) Panel (a) is identical to Fig. 3(c), but now for each transition-energy line we specify the initial and final states, with respective energies $\varepsilon^{k'}_N$ and ε^k_{N+1}, between which the transition occurs. Recall that k is an index which numbers states in a given spin multiplet with respect to energy, with $k = 0$ denoting the ground state. Moreover, by labeling the lines with (k,k') we mean that k refers to the final state of a charged SMM ($N+1$), whereas k' represents the initial state of a neutral SMM (N). We note that information shown in (a) cannot be readily seen from energies ε^k_n ($n = N, N+1$) of the individual levels, which for the completeness of the present discussion are plotted in (b). Observe that since energies in (b) are calculated at the Coulomb resonance, the curves for $k = 0$ overlap.

leads to an enhancement of $G_{\max}$ for $B \lesssim 3.25$ T, followed by a steady decrease, i.e., the characteristic nonmonotonic behavior experimentally observed in Fig. 2(a). We emphasize that the above mechanism does not constitute a purely spectroscopic method: The current and probabilities depend on both the *energies* and *quantum states*, which determine the tunnel rates. The importance of including many excited states in the calculation is quantified in Fig. 3(d), where we show how the nonmonotonic behavior can be strongly overestimated when including too few excited states; see also Figs. 13–16. We note that some additional remarks regarding signatures of the transverse anisotropy parameter E in the peak amplitude of $G_{\max}$ are discussed in Appendix B4.

Finally, worth noting is the larger-than-predicted modulation of the CP amplitude observed in the experiments. We briefly comment on the verifications to rule out some other contributions that could lead to such an amplification. First, the master equation analysis was constrained to a weak tunnel-coupling Γ as compared to temperature. We verified that higher-order tunnel processes that lead to broadening and inelastic tunneling do not increase the scale of the modulation of the CP height. For this we employed a perturbative approach including next-to-leading tunneling processes [30] and a nonperturbative numerical renormalization group (NRG) method [31–33]. Second, we assumed symmetric tunnel coupling of the SMM to both electrodes with the same energy Γ. One can show that a junction asymmetry gives rise to an overall constant factor suppressing the conductance $G_{\max}$. Thus, this cannot change its field dependence. Third, the addition of higher-order magnetic anisotropy terms to the SMM model, Eq. (2), is also not likely to affect the magnitude of the modulation. We checked, for instance, the effect of the fourth-order transverse anisotropy of the form $C_n[(\hat{S}^x_n)^4 - (\hat{S}^y_n)^4]$, for a range of values of the parameter $C_{N/N+1}$ for which this term competes with the second-order transverse term. We thus conclude that the intensity of the modulation may rely on some intrinsic amplification mechanism not captured by our model, i.e., going beyond the giant-spin model [19,34], when considering a single electron interacting with the molecule.

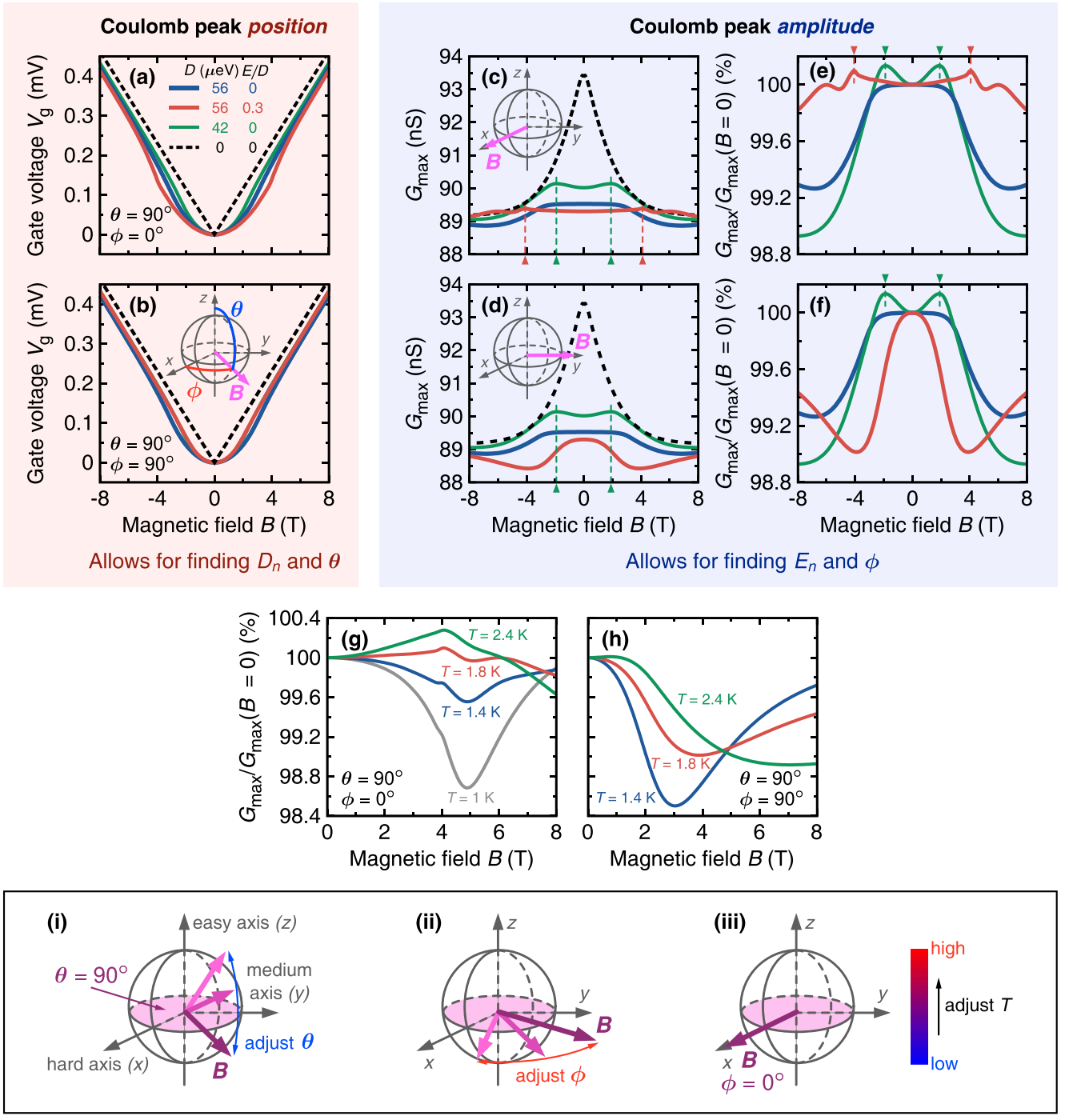

FIG. 5. (Color online) How to determine the transverse magnetic anisotropy constant E of an individual SMM from its transport characteristics. The *position* (a),(b) and *amplitude* (c)–(f) of the CP are shown for different values of the parameters D and E of the SMM model with $S_N = 5$ and $S_{N+1} = 9/2$ for $T = 1.8$ K. Note that we employ the assumption for the Fe_4 molecule from the main text, that is, $D = D_N = D_{N+1}/1.2$ and $E = E_N$, with $E_N/E_{N+1} = D_N/D_{N+1}$, and a relatively large value of E/D (red lines) is used for clear illustration of the effects under discussion. In panels (a),(c),(e) the external magnetic field $\boldsymbol{B}$ is oriented along the SMM's *hard* axis x [see inset in (c)], whereas in panels (b),(d),(f) the field is parallel to the *intermediate* axis y [see inset in (d)]. In panel (g) we present how temperature affects the occurrence of characteristic peaks associated with the presence of transverse magnetic anisotropy for $\boldsymbol{B}$ along the *hard* axis x; for further details, see Fig. 16. To make the discussion complete, in panel (h) we show analogous dependencies but in the case when the field lies along the *intermediate* axis y. Finally, the frame at the bottom contains a schematic summary of the procedure leading to estimation of E: (i) Using the analysis of the CP *position*, find D_n and adjust the magnetic field $\boldsymbol{B}$ so that it is contained in the hard plane, i.e., the plane perpendicular to the easy axis z. (ii) Rotating systematically the magnetic field $\boldsymbol{B}$ in the hard plane, analyze the CP *amplitude* to find the direction of the molecule's hard axis. This will be characterized by the occurrence of additional peaks in the amplitude, whose field position allows for estimating E_n. (iii) If no local maxima in the amplitude can be seen, adjust (try increasing) the temperature.

V. FITTING PROCEDURE: HOW TO FIND ANISOTROPY PARAMETERS OF A SINGLE MOLECULE FROM ITS TRANSPORT SPECTRA

We summarize here in a few steps how to determine magnetic anisotropy of an individual SMM [see Eqs. (1) and (2) and Appendix B1) by exploiting the information contained both in the CP *position* as well as in the magnetic field evolution of its *amplitude*. In particular, the method under discussion allows for finding both the magnetic anisotropy constants D_n and E_n in two charge states (i.e., for $n = N, N+1$) of an SMM and the orientation of an external magnetic field relative to the molecule's principle axes, given by the angles θ and ϕ.

(i) Let us first consider only the CP *position*, shown in the left panel of Fig. 5. As explained in Ref. [24], by analyzing the position of the CP one can immediately conclude whether a molecule captured in the junction exhibits magnetic anisotropy at all. If the molecule is *spin isotropic*, one observes a linear dependence on the magnetic field [see dashed line in Figs. 5(a) and 5(b)] that reflects the linear Zeeman effect. On the other hand, if the molecule is *spin anisotropic*, this dependence becomes nonlinear, and the uniaxial magnetic anisotropy parameter D_n together with the angle θ can be estimated from it. This, in turn, permits for systematic adjustment of the magnetic field's orientation so that the field is kept perpendicular to the molecule's easy axis z, which corresponds to $\theta = 90^\circ$.

(ii) The transverse magnetic anisotropy breaks the molecule's rotational symmetry around the easy axis z (see also Appendix B2). In consequence, one expects that such a symmetry breaking should manifest itself in different transport characteristics of the system occurring for various orientations of the magnetic field in the hard plane (i.e., the plane perpendicular to the easy axis). From Figs. 5(a) and 5(b) it is clear that the sole position dependence in practice does not allow one to derive reliably either the transverse magnetic anisotropy constant E_n or the angle ϕ. For this purpose, also the *amplitude* of the CP has to be taken into consideration.

(iii) The presence of transverse magnetic anisotropy can be confirmed by observation of how the field dependence of the CP amplitude changes when rotating the field orderly in the hard plane, or, in other words, by varying the angle ϕ. Specifically, one should notice then *two* significantly different shapes of the amplitude showing up every 90°; cf. red lines with others in the right panel of Fig. 5. These two limiting cases represent the situation when the magnetic field lies either along the molecule's hard axis x ($\phi = 0^\circ$ or $\phi = 180^\circ$), Figs. 5(c) and 5(e), or along the molecule's intermediate axis y ($\phi = 90^\circ$ or $\phi = 270^\circ$), Figs. 5(d) and 5(f). Consequently, this enables one to determine the approximate value of the angle ϕ.

(iv) The effect of transverse magnetic anisotropy on the CP amplitude should be most pronounced for the magnetic field aligned along the molecule's hard axis x; see Appendix B2 and Figs. 2(c) and 2(d). For a sufficiently high temperature T [see Figs. 5(f) and 5(g) and Fig. 16] and observes then formation of local maxima, marked by red arrows in Figs. 5(c) and 5(e), from whose position the value of the transverse magnetic anisotropy constant E_n can be numerically estimated.

Importantly, the method under discussion relies on a simultaneous fitting of *position* (sensitive to D_n) and the *amplitude* (sensitive both to D_n and E_n) of the CP. This strictly limits the freedom of the parameters' choice, basically leaving E_n to be determined from the field value at which the maximum amplitude is acquired. For instance, making the parameters D_n smaller by 25% than the one used above (given the fixed experimental temperature $T = 1.8$ K), while assuming $E_n = 0$, may also produce a maximum; see green lines in Figs. 5(c) and 5(f). However, not only does it result in peak positions at completely wrong magnetic fields [cf. position of green and red arrows in Fig. 5(e)], but also the amplitude shape remain unaltered upon changing the orientation of the field in the hard plane [cf. red and green lines between Figs. 5(e) and 5(f)]. This restriction, combined with the sensitivity of the qualitative curve shape of the conductance to the parameters is advantageous for extracting the anisotropy parameters of SMMs *in situ*.

VI. CONCLUSIONS

In conclusion, we have proposed a new method of probing the transverse magnetic anisotropy of an individual SMM embedded in a three-terminal device. It exploits the information contained in the spin states of the molecule through the analysis of the magnetic field evolution of the linear conductance amplitude $G_{\max}$. We found that the evolution of $G_{\max}$ in a magnetic field could only be reproduced when including a sufficient number of excited states. Estimates for the transverse anisotropy of the Fe_4 SMM yield $E \approx 0.17D = 9.5\ \mu$eV, a value of E significantly larger than the observed bulk/monolayer values. This is expected for a molecule captured in the low-symmetry environment of a transport junction. Importantly, the technique does not rely on the small induced tunneling effects and hence works well at temperatures by far exceeding the tunnel splittings and even E itself. Our measurements find larger modulation of $G_{\max}$ than calculated and the origin of this enhancement requires further study. This method may facilitate the detection of *in situ* mechanical tuning [3] or excitation [35,36] of magnetic anisotropy of a single molecule.

ACKNOWLEDGMENTS

This work was supported by NWO (VENI) and OCW, and by EU FP7 Project No. 618082 ACMOL and an advanced ERC grant (Mols@Mols). M.M. acknowledges financial support from the Alexander von Humboldt Foundation. K.P. was supported by U.S. National Science Foundation Grant No. DMR-1206354.

APPENDIX A: MATERIALS AND EXPERIMENTAL METHOD

1. Details of the Fe_4 single-molecule magnet

We used an Fe_4 SMM with formula $[Fe_4(L)_2(dpm)_6]\cdot Et_2O$ where Hdpm is 2,2,6,6-tetramethyl-heptan-3,5-dione and H_3L is the tripodal ligand 2-hydroxymethyl-2-phenylpropane-1,3-diol, which carries a phenyl substituent [20]. In the bulk phase, the crystallographic symmetry is C_2 [20]. The magnetic core

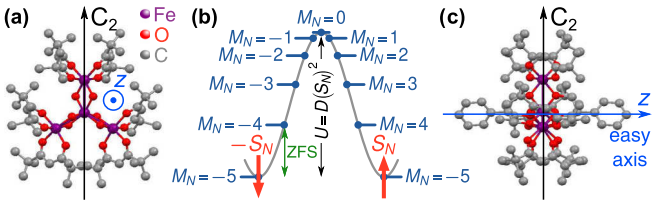

FIG. 6. (Color online) Details of the Fe_4 SMM. (a) Sketch of the magnetic core of the Fe_4 SMM. (b) Ground-state spin multiplet ($S_N = 5$) of the Fe_4 SMM in a neutral charge state N; for further explanation see Appendix B2. (c) Depiction of the Fe_4 SMM illustrating the orientation of the phenyl rings [omitted in (a)] that terminate the molecule. Note that in both (a) and (c) hydrogen atoms are disregarded for clarity.

of the Fe_4 SMM is made of 4 Fe^{3+} ions (each with spin $s = 5/2$) as illustrated in Fig. 6(a). The antiferromagnetic exchange interaction between the central and peripheral ions yields a large molecular spin $S_N = 5$ in the ground state. Magnetic anisotropy due to the interaction with the crystal field lifts the degeneracy of the spin multiplet into five doublets and one singlet that are distributed over an energy

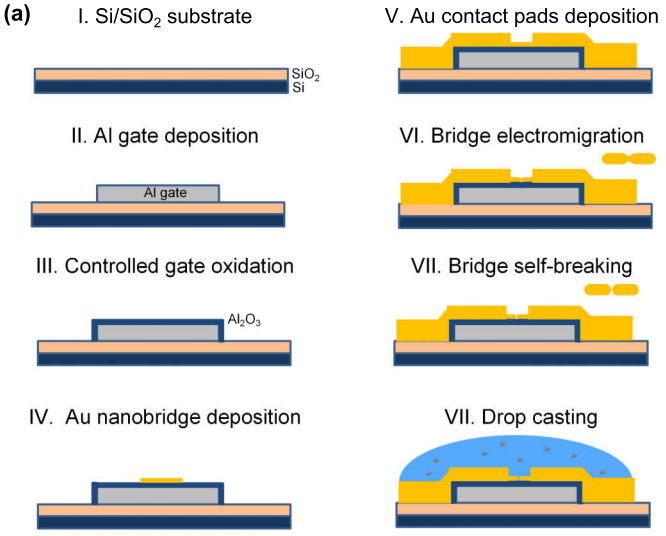

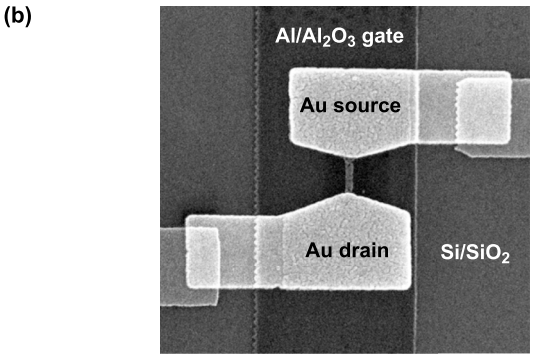

FIG. 7. (Color online) Three-terminal-junction fabrication. (a) Schematics of the three-terminal-device fabrication process. (b) Scanning electron microscope (SEM) image of a real three-terminal device before electromigration.

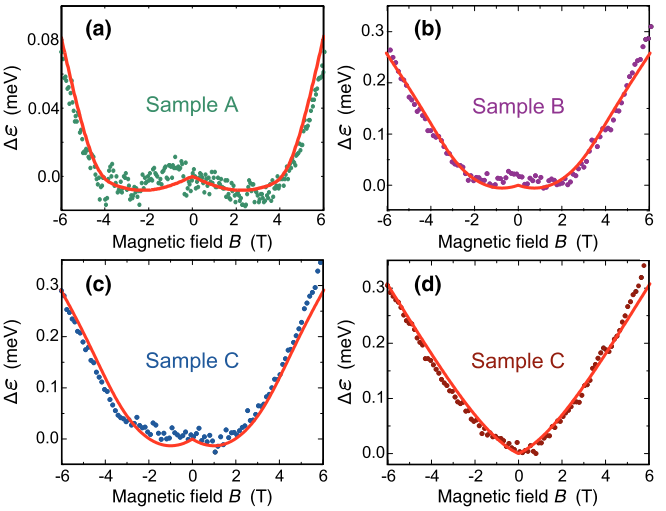

FIG. 8. (Color online) Coulomb peak position gate-voltage spectroscopy. The shift of the CP position due to magnetic field for samples A, B, and C. The solid lines are fits to $\varepsilon^0_{N+1} - \varepsilon^0_N$, calculated from the giant-spin Hamiltonian, Eqs. (1) and (2). From the fit we get the following values: for sample A in (a), $D_{N+1} = 61$ μeV, $\theta_N = 87°$, and $\theta_{N+1} = 86°$; for sample B in (b), $D_{N+1} = 65$ μeV, $\theta_N = 86°$, and $\theta_{N+1} = 84°$; for sample C, in (c) $\theta_N = 87°$ and $\theta_{N+1} = 85°$, whereas in (d) $\theta_N = 63°$ and $\theta_{N+1} = 62°$, with $D_{N+1} = 68$ μeV in both cases. We note that the evolution of the CP position in magnetic field, and not G_{max}, for samples A and C was previously analyzed in Ref. [24]. Also note that in the fitting for sample A we included $E/D = 0.2$ and $\phi = 0°$ obtained in Fig. 2.

barrier as shown in Fig. 6(b); for further discussion see Appendix B2. The height of the barrier, which hinders the spin reversal, is given by $U = D(S_N)^2$, where D is the uniaxial magnetic anisotropy parameter. In the case of bulk Fe_4 the height is $U = 1.4$ meV [20]. The ZFS, defined as the energy difference between the two lowest-lying doublets ($M_N = \pm 5$ and $M_N = \pm 4$) is 0.5 meV. The low symmetry of the molecule induces a transverse magnetic anisotropy E that, in bulk, is $E = 2.85$ μeV from EPR measurements [20]. Finally, we note that the molecule contains two axial tripodal ligands L^{3-} which hold the core together and six peripheral dpm^- ligands that create an hydrophobic envelope; see Fig. 6(c).

2. Details on the fabrication methods of the three-terminal junctions

The three-terminal junctions are fabricated on a silicon substrate covered by 280 nm of SiO_2. The schematics of the fabrication process is described in Fig. 7(a). The gate electrode is fabricated by e-beam lithography and subsequent e-beam deposition of Al. In the next step, the oxidation of the gate in a controlled oxygen atmosphere produces a dielectric coating layer of 2–3 nm of Al_2O_3. The source and drain electrodes are fabricated by self-breaking, controlled electromigration of a Au nanobridge deposited by e-beam lithography on top of the oxidized gate. The self-breaking technique prevents the formation of gold nanograins in the junction that could mimic the behavior of a molecule. Figure 7(b) shows a scanning electron microscope image of a device before electromigration.

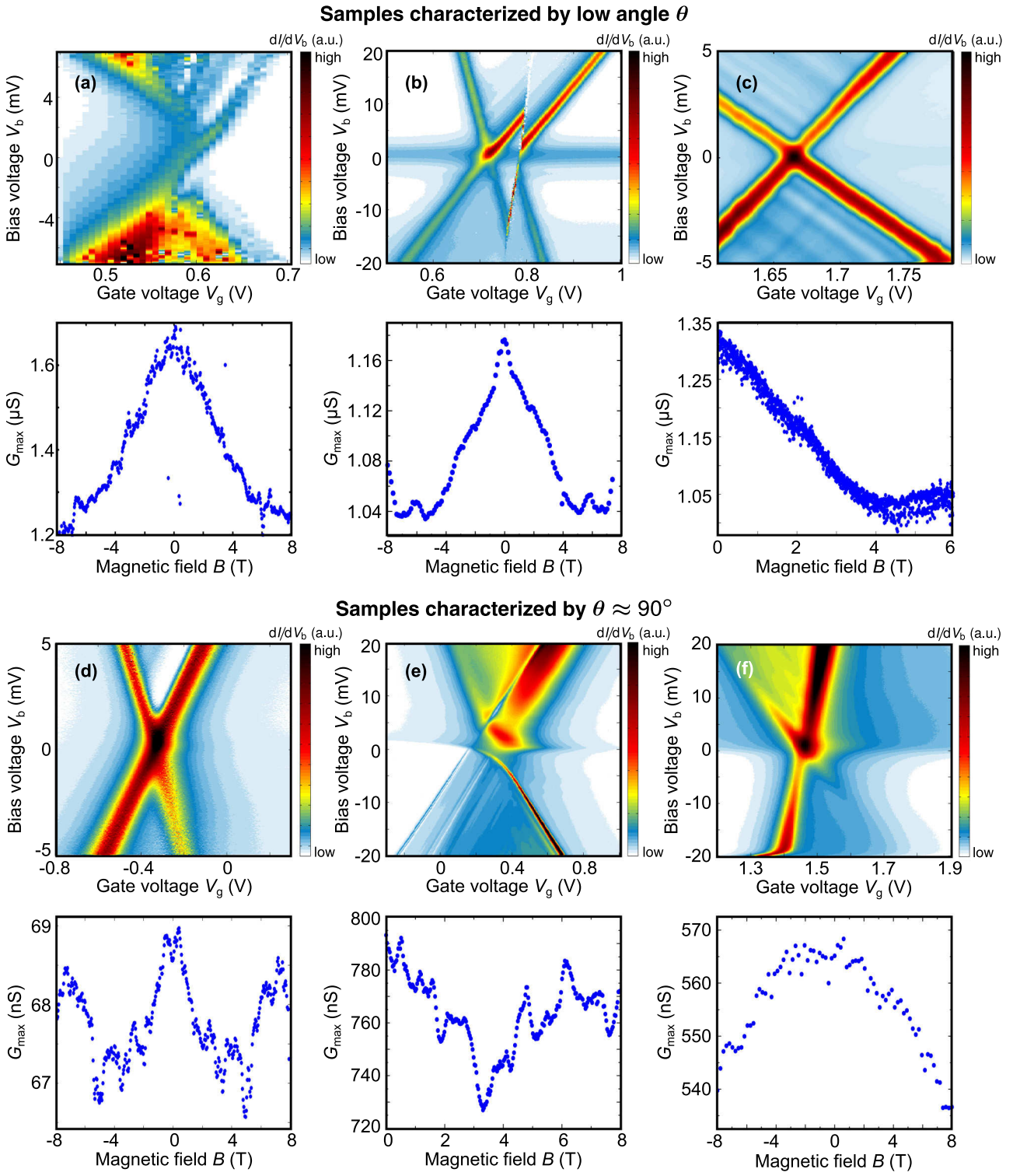

FIG. 9. (Color online) Statistics. Differential-conductance maps, dI/dV_b, shown as a function of gate V_g and bias V_b voltages together with corresponding dependencies of the CP amplitude G_{max} on magnetic field B for six different Fe_4 molecular junctions. (Top) [(a)–(c)] Junctions for which gate-voltage spectroscopy fits of the CP position (not shown) indicate $\theta < 60°$. (Bottom) [(d)–(f)] Junctions where $\theta \approx 90°$ is found. The shape of the field modulation of G_{max} implies that for (d) and (e) the field is close to the intermediate axis ($\phi \approx 90°$), whereas for (f) it is most likely in an intermediate ϕ angle in the hard plane.

The molecules are deposited onto the chip by drop casting a 10^{-4} M solution in toluene into a liquid cell containing the chip with the junctions. The electromigration of the bridge and subsequent self-breaking are carried out in solution to maximize the yield of junctions with a molecule.

3. Details on the gate-voltage position spectroscopy

The molecule-electrode coupling Γ is estimated from the broadening of the Coulomb edge at low bias. In particular, the full width at half maximum of the CP is used for this purpose. We find 1.6, 2.0, and 1.4 meV for samples A, B, and C, respectively. Note, however, that these values are an upper limit for Γ since we cannot resolve the presence of additional components for the broadening such as thermal energy or the contribution of other molecular levels very close in energy.

Figure 8 shows the CP position in gate voltage V_g as a function of the magnetic field for the samples A, B, and C described in the main text and Figs. 2(a) and 2(b). The values of V_g are multiplied by the gate coupling β to obtain energy units ($\Delta\varepsilon$) and subsequently rescaled to make $\Delta\varepsilon = 0$ for $B = 0$. The nonlinearity of the field dependence is a clear signature of the magnetic anisotropy as described in the main text (see also Ref. [24]). Moreover, the low-field "flatness" of $\Delta\varepsilon$ observed in Figs. 8(a)–8(c) is indicative of a high value of θ in contrast with Fig. 8(d). The solid lines in Fig. 8 are a fit of the data to $\Delta\varepsilon = \varepsilon^0_{N+1} - \varepsilon^0_N$ as defined by the giant-spin Hamiltonian, Eqs. (1) and (2), and also discussed in detail in Appendix B1. The CP position is mainly insensitive to E (see also Supporting Information in Ref. [24]), and therefore we can independently extract the parameters D and θ related to the uniaxial anisotropy. Note that we fix the value of D_N (neutral state) to the bulk value $D_N = 56\ \mu$eV and thus the free parameters are D_{N+1}, θ_N, and θ_{N+1}. See the caption of Fig. 8 for the fitting values of these parameters.

4. Statistics and effect of the magnetic field polarity

We measured around 200 electromigrated junctions, from which 17 showed molecular signatures. A total of 9 molecular junctions displayed a clear CP suitable for further analysis by means of the gate-voltage spectroscopy method, from which the junctions were proven to exhibit magnetic anisotropy. Importantly, all these junctions displayed a modulation of the peak amplitude G_{max} as a function of the magnetic field. A total of 6 of these samples could be rotated or were close to $\theta = 90^\circ$. From those, one sample was close to $\phi = 0^\circ$ (hard axis), and it is referred to as sample A. Figure 9 shows the differential-conductance maps, dI/dV_b, and corresponding magnetic field evolutions of G_{max} for different Fe_4 molecular junctions, that is, other than samples A, B, and C discussed in the main text. The top panel [(a)–(c)] of Fig. 9 presents samples for which the gate spectroscopy yields low values of θ. Worthy of note is that for $|B| < 4$ T a decrease of G_{max} is observed with increasing $|B|$. On the other hand, the bottom panel [(d)–(f)] of Fig. 9 shows examples where $\theta \approx 90^\circ$ (i.e., close the the hard plane). The shape of G_{max} for (d) and (e) indicates that the magnetic field is close to the intermediate axis ($\phi \approx 90^\circ$), which follows from the analysis carried out in the main text. For the last sample, Fig. 9(f), the field is most likely at an intermediate angle ϕ in the hard plane.

In order to discard the influence of universal conductance fluctuations induced by the magnetic field in the measurements, in Fig. 10 we plot G_{max} as a function of B for the samples shown in Figs. 2(a) and 2(b) for both positive and negative polarities of magnetic field. We note that the main features, like the minima or maxima around 4 T, are

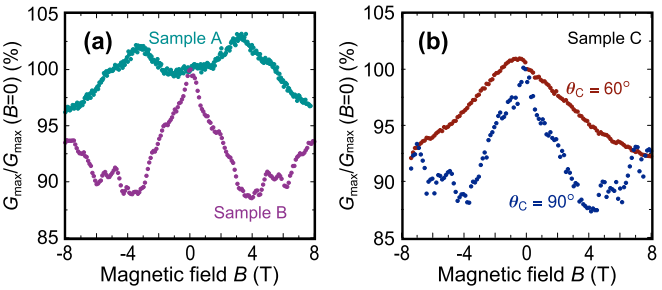

FIG. 10. (Color online) The effect of the reversed magnetic field polarity on G_{max}. Dependence of the scaled CP height $G_{max}/G_{max}(B = 0)$ on magnetic field B for the samples discussed in the main text, cf. Figs. 2(a) and 2(b), showing that the curves are symmetric upon reversal of the field polarity.

reproducible under inversion of the field polarity. Universal conductance fluctuations are not expected to be symmetric by changing the B polarity. Some additional symmetric structure appears also in the measurements. The analysis of this smaller contribution is interesting but beyond the scope of this work.

If present, conductance fluctuations would equally appear in the zero-bias and the higher-bias conductance. Therefore, in order to rule out their presence, we have analyzed the magnetoresistance at higher biases and different gate voltages. Figure 11 shows differential conductance, dI/dV_b, as a function of B measured at two different bias V_b voltages (for a fixed gate V_g voltage) in the Coulomb blockade in sample A. We observe an almost flat response of dI/dV_b with peak-to-peak variation of the order of 0.1 nS. This magnitude is not comparable to the modulations we attribute to the presence of the transverse anisotropy. Moreover, note that these two spectra are not symmetric by reversing the magnetic field polarity. Thus, we conclude that the universal conductance fluctuations are not significant in our measurements.

APPENDIX B: THEORETICAL MODELING

1. Charge-dependent, giant-spin-based model of an single-molecule magnet

The central element of the theoretical description of the gate-spectroscopy technique is a proper choice of the model

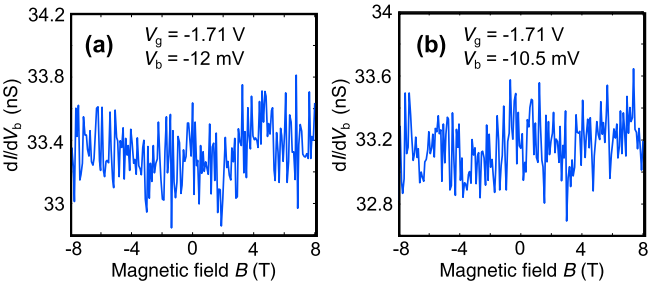

FIG. 11. (Color online) Cotunneling background. Differential conductance, dI/dV_b, measured as a function of magnetic field B at two different points: (a) $V_g = -1.71$ V and $V_b = -12$ mV and (b) $V_g = -1.71$ V and $V_b = -10.5$ mV, which correspond to the cotunneling background in the left-hand charge state of sample A; cf. Fig. 1(c).

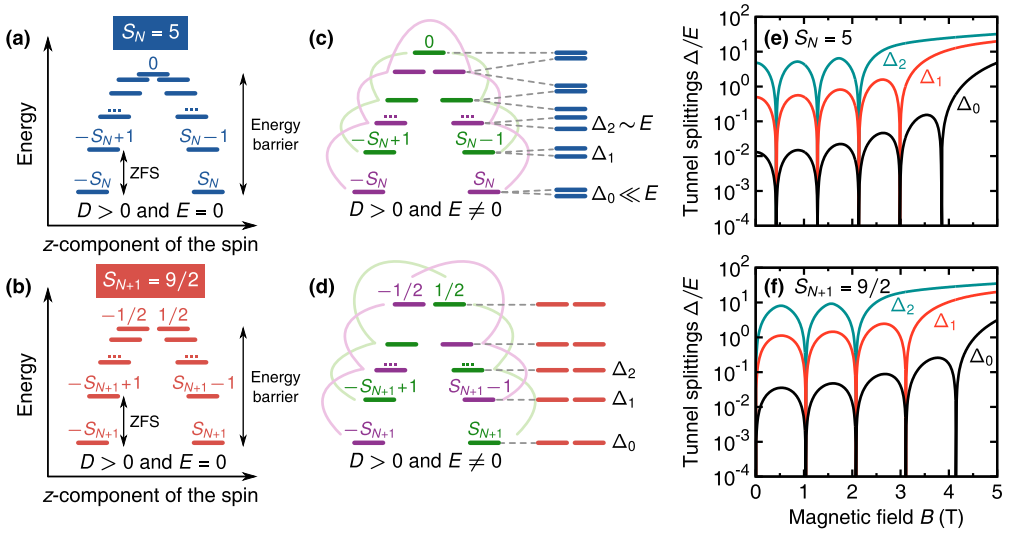

FIG. 12. (Color online) Effect of magnetic anisotropy on the energy spectrum of SMM. (Top)/(Bottom) [(a,c,e)/(b,d,f)] The case of a *integer/half-integer* value of a molecular spin. In particular, we use the values of spin known for a Fe_4 SMM, $S_N = 5$ for a neutral molecule and $S_{N+1} = 9/2$ for a charged one [5]. (a),(b) In the presence of exclusively *uniaxial* magnetic anisotropy $D > 0$ (and without magnetic field, $B = 0$) an energy barrier protecting the molecule's spin against reversal between two opposite, energetically degenerate, orientations arises. The excitation between the ground-state doublet and the first excited doublet is then commonly referred to as the ZFS. (c),(d) If additionally the *transverse* component of magnetic anisotropy occurs, it allows for mixing of pure S_z states. Each new eigenstate is then formed from S_z states belonging to one of two uncoupled, time-reversed sets, as schematically marked by two different colors. As follows from the Kramers theorem, for $S_N = 5$ the transverse magnetic anisotropy introduces tunnel splittings Δ, whereas for $S_{N+1} = 9/2$ all states remain doubly degenerate. (e),(f) A characteristic feature of such anisotropic, large spins is that when an external magnetic field B is applied along the system's hard axis, one observes periodic changes of the tunnel splittings [1,14]. Other parameters assumed in the calculations: $D_N = 56\ \mu$eV, $D_{N+1} = 68\ \mu$eV, and $E_N/D_N = E_{N+1}/D_{N+1} = 0.3$.

capturing essential features of an SMM. As introduced in the main text (see Sec. IV), the molecule is represented by a model based on two giant-spin Hamiltonians [1,37,38]. This allows us to take into account the fact that by tuning a gate voltage V_g the molecule can be switched between two different charge states [5], referred to as *neutral* (N) and *charged* ($N+1$). In general, each of this states can be characterized not only by different values of molecular ground-state spin (S_N and S_{N+1}), but also uniaxial (D_N and D_{N+1}) and transverse (E_N and E_{N+1}) magnetic anisotropy constants. Using the spin raising/lowering operators $\hat{S}_n^{\pm}$, the Hamiltonian of an SMM in the charge state n and subject to an arbitrarily oriented external magnetic field $\boldsymbol{B}$ takes the form given by Eqs. (1) and (2) and the Zeeman term explicitly given by

$$\hat{\mathcal{H}}_n^{\mathrm{Z}} = g\mu_{\mathrm{b}}B\left[\tfrac{1}{2}\hat{S}_n^{+}\sin\theta\, e^{-i\phi} + \tfrac{1}{2}\hat{S}_n^{-}\sin\theta\, \mathrm{e}^{i\phi} + \hat{S}_n^{z}\cos\theta\right], \tag{B1}$$

with the angles θ and ϕ defined as illustrated in Fig. 1(b). Noteworthily, by keeping the same value of θ and ϕ for both charge states, we implicitly assume that the orientation of the molecule's principle axes set by magnetic anisotropy is not affected by charging. This assumption does not necessarily hold for real systems as shown in Refs. [5] and [24]. However, since the tilting, if observed, usually does not exceed few degrees, we do not include such an effect into the present considerations.

2. How does magnetic anisotropy affect the energy spectrum of a large spin?

Before we analyze how electronic transport probes the transverse magnetic anisotropy of a molecule, it may be instructive first to discuss the consequences of the transverse magnetic anisotropy and external magnetic field for the SMM's energy spectrum.

To begin with, as long as the transverse magnetic anisotropy is vanishingly small the system can be described simply by the first term of the Hamiltonian (2). As a result, the eigenvalues M_n of the spin operator $\hat{S}_n^z$ become good quantum numbers for labeling the eigenstates of $\hat{\mathcal{H}}_{\mathrm{SMM},n} = -D_n(\hat{S}_n^z)^2$, that is, $\hat{\mathcal{H}}_{\mathrm{SMM},n}|M_n\rangle = -D_n M_n^2|M_n\rangle$. For $D_n > 0$ the energy spectrum of an SMM takes the form of an inverted parabola with an energy barrier of height $\sim D_n S_n^2$ for spin reversal, which basically corresponds to the indirect transition between the ground states $|-S_n\rangle$ and $|S_n\rangle$ by climbing the barrier *via* the intermediate states $|M_n\rangle$ (for $M_n = -S_n+1,\ldots,S_n-1$); see Figs. 12(a) and 12(b). Importantly, the excitation energy between the ground state $|\pm S_n\rangle$ and the first excited state $|\pm S_n \mp 1\rangle$, ZFS $= (2S_n - 1)D_n$, sets the threshold energy scale for the reversal process to take place. Note that transition energies between neighboring excited states $|M_n\rangle$ and $|M_n'\rangle$ with $|M_n - M_n'| = 1$ are characterized by energies $(2M_n - 1)D_n$ (for $0 < M_n < S_n$) that are smaller than the ZFS, and these states remain generally unpopulated until the ground-to-first excited-state transition becomes energetically permitted. This bottleneck behavior manifests then in electronic transport

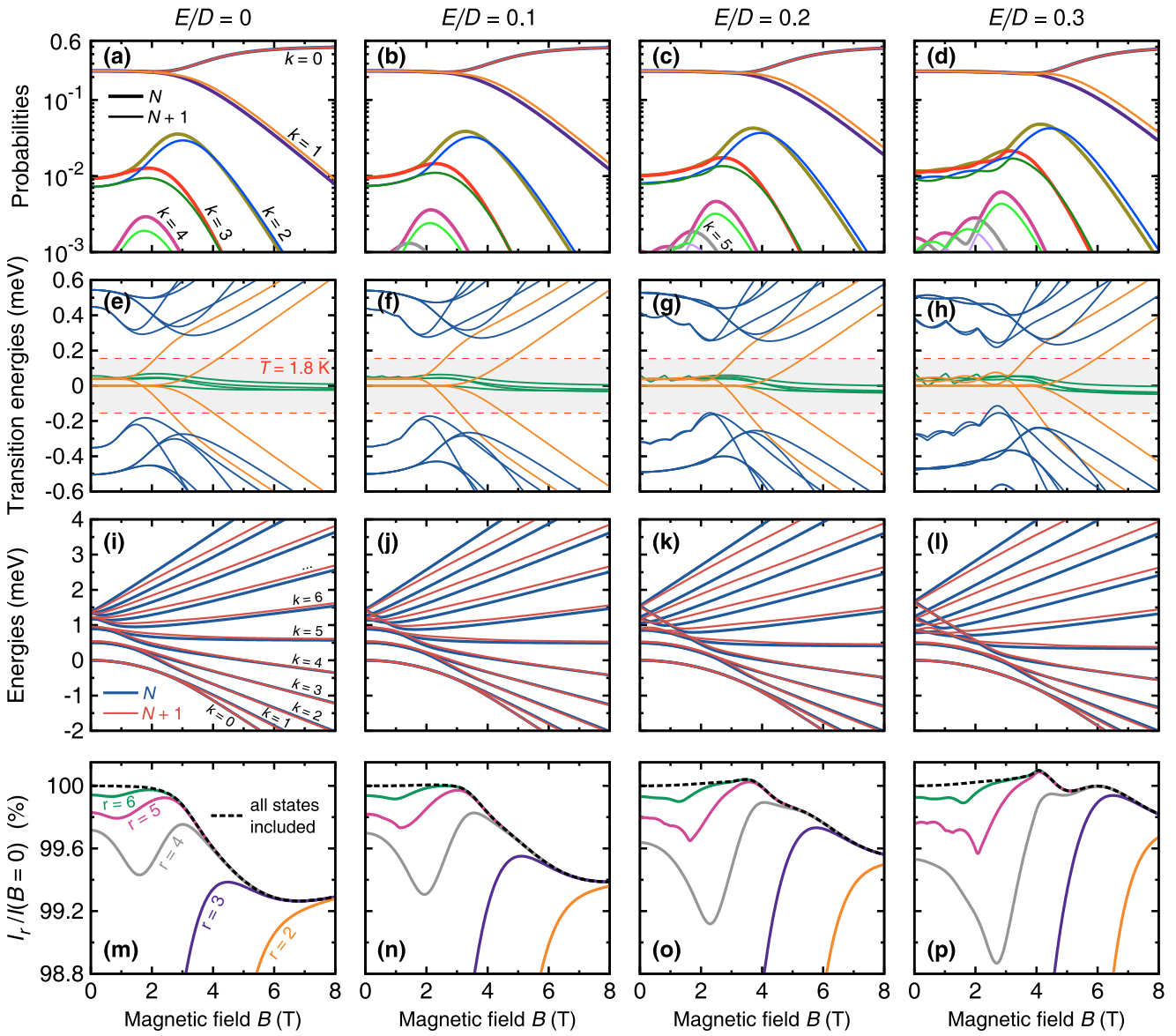

FIG. 13. (Color online) Signatures of the transverse magnetic anisotropy in electronic transport (magnetic field along the *hard* axis, $\theta = 90^\circ$ and $\phi = 0^\circ$). Analogous to Figs. 3(b)–3(d) with each column corresponding now to a different value of E/D: (a)–(d) occupation probabilities for several lowest-in-energy states in the spin multiplets for N and $N+1$ at $T = 1.8$ K; (e)–(h) transition energies $\varepsilon^k_{N+1} - \varepsilon^{k'}_N$ relevant for the SET processes at the Coulomb resonance (i.e., $\varepsilon^0_{N+1} = \varepsilon^0_N$ is restored for each B by tuning V_g) for $k,k' \leq 4$. Different colors of lines are used to distinguish groups of transitions with respect to possible combinations of indices k and k' [see the discussion regarding Figs. 3(c) and 4; (i)–(l) energies ε^k_n for $n = N, N+1$ at the Coulomb resonance (observe that the curves for $k = 0$ overlap); (m)–(p) Dependence of the current on the number of spin-multiplet states r included from each charge state. The left (right) most column represents the case of absent (significant) transverse magnetic anisotropy. Importantly, each column shows a detailed analysis of selected conductance curves from Fig. 2(c). We note that transition-energy lines in (e)–(h) can be easily identified with the use of Fig. 4(a). It can be seen that increasing E/D results in shifting the minima of the transition-energy curves in (e)–(h) towards higher values of the field. Such a behavior, in turn, affects the occupation probabilities (a)–(d), so that the probability of finding an SMM in either the ground ($k = 0$) or the first excited ($k = 1$) state for both charge states N and $N+1$ remain equal for a larger magnetic-field range (compare the outermost columns). Recall that the position of the CP is fixed mostly by D; see Fig. 8.

through an SMM, where it can be observed as a steplike feature in the conductance only at bias voltages $V_b = \pm \mathrm{ZFS}/|e|$ [5,13].

The relatively simple picture presented above is not valid, however, if the transverse magnetic anisotropy (or an external magnetic field perpendicular to the molecule's easy axis) is significant. When $E \neq 0$, the second term of the Hamiltonian (2) breaks the system's rotational symmetry around the easy axis z, so that M_n is no longer a good quantum number. In fact, each of the $2S_n + 1$ eigenstates of $\hat{\mathcal{H}}_n = -D_n(\hat{S}^z_n)^2 + (E_n/2)[(\hat{S}^+_n)^2 + (\hat{S}^-_n)^2]$ is now a linear combination of the eigenstates $|M_n\rangle$, which, in turn, underlies the origin of the

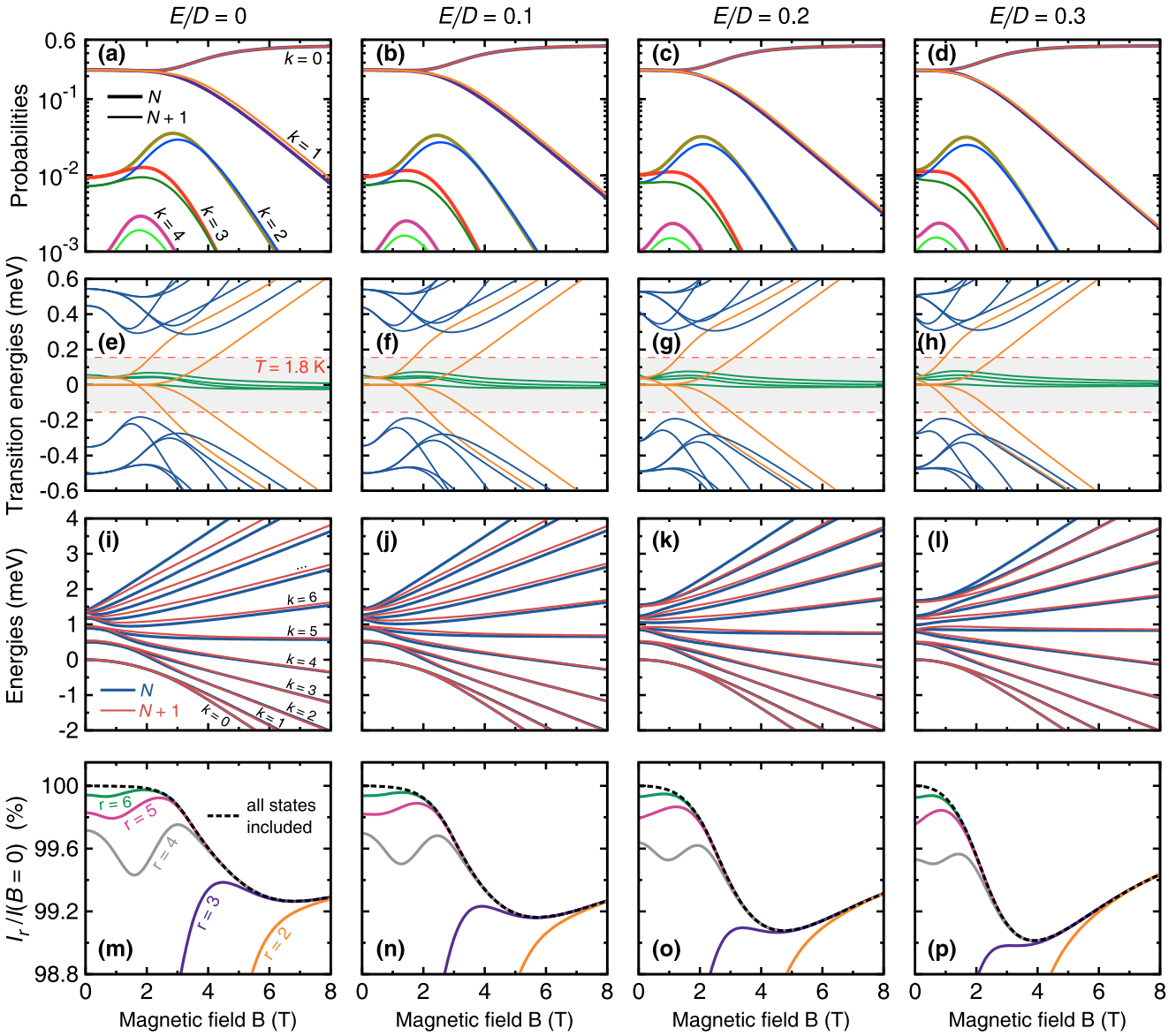

FIG. 14. (Color online) Signatures of the transverse magnetic anisotropy in electronic transport (magnetic field along the *intermediate* axis, $\theta = 90^\circ$ and $\phi = 90^\circ$). Generally, this figure is analogous to Fig. 13, except that now the external magnetic field is rotated to align with the molecule's intermediate (y) axis. To begin with, we note that the results shown in the leftmost column (i.e., for $E/D = 0$) are identical to those in the leftmost column of Fig. 13, which is the manifestation of the molecule's rotational symmetry about the easy (z) axis in the absence of transverse component of magnetic anisotropy. Unlike for the case of $\phi = 0^\circ$, the consequence of the increase of E/D is the displacement of the transition-energy curves minima (e)–(h) towards smaller values of the field. Interestingly enough, in the situation under discussion one thus observes a more abrupt decrease of the current [see dashed lines in (m)–(p)] for larger E/D occurring at smaller values of B.

quantum tunneling of magnetization [12]. In particular, each of these eigenstates is formed from states $|M_n\rangle$ belonging to one of two uncoupled, time-reversed sets, as shown in Figs. 12(c) and 12(d). For an *integer* spin S_n, the transverse magnetic anisotropy leads to splitting of energy levels, usually referred to as *tunnel splittings*, Fig. 12(c), whereas for a *half-integer* spin S_n (in the absence of magnetic field), according to the Kramers theorem, each energy level is doubly degenerate, Fig. 12(d). Interestingly, if one applies an external magnetic field in the direction perpendicular to the system's easy axis z, periodic changes of these tunnel-splittings can be observed if the field is oriented along or close the hard axis x, Figs. 12(e) and 12(f), and they disappear as the field gets rotated towards the direction of the intermediate axis y [1,12,14].

3. Transport in the single electron tunneling regime

For a weak tunnel coupling between an SMM and electrodes, transport in the single electron tunneling (SET) regime can be considered in the leading-order perturbative approach (Fermi golden rule combined with a master equation) [16,28,29].

We describe metallic, *nonmagnetic* electrodes [$q = (L)$eft,(R)ight] as reservoirs of noninteracting electrons,

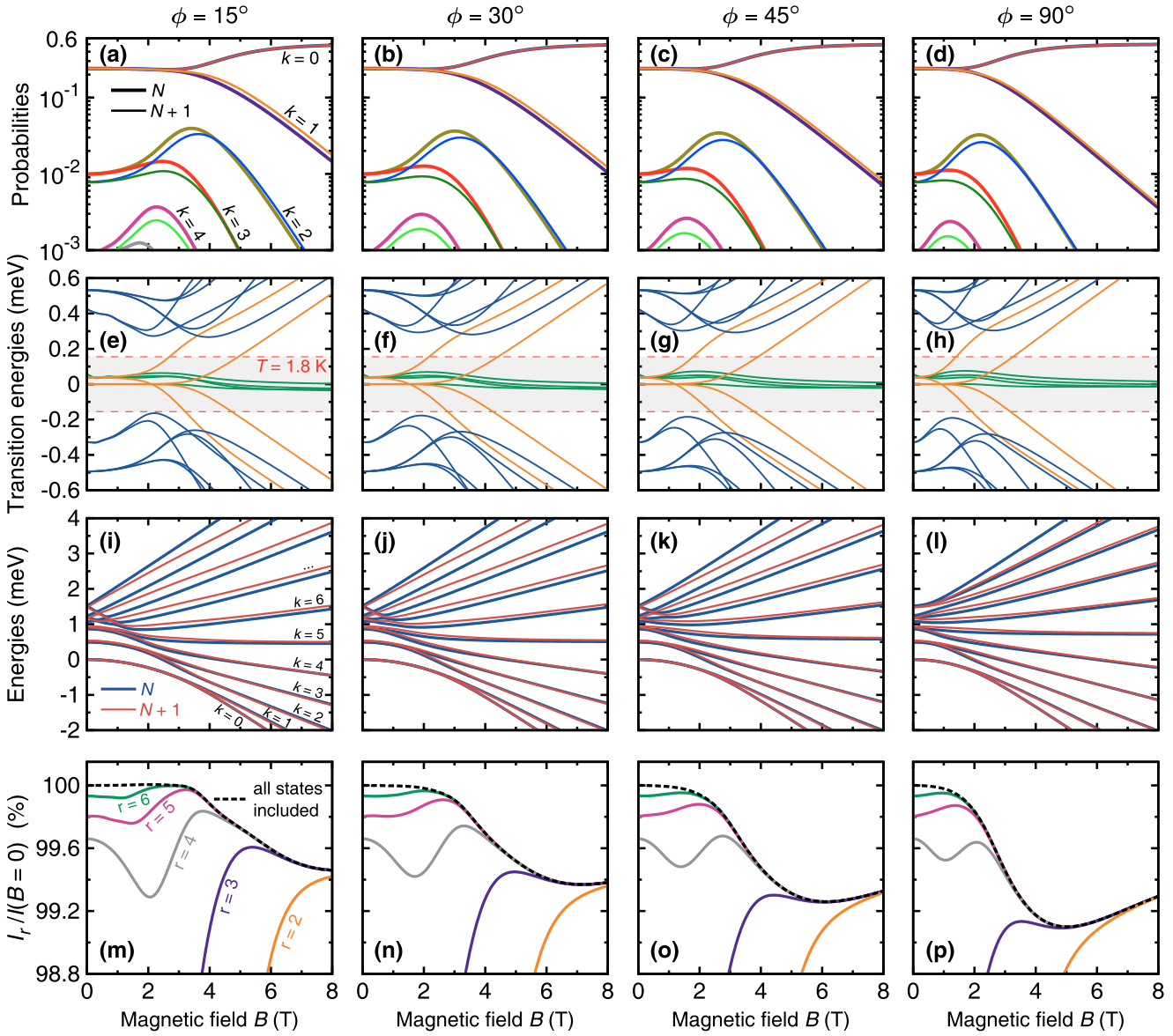

FIG. 15. (Color online) Dependence of transport signatures of the transverse anisotropy on the orientation of magnetic field in the *hard* plane ($\theta = 90°$) for $E/D = 0.17$. Analogous to Figs. 3(b)–3(d), with each column corresponding now to a different value of ϕ. Note that the case of $\phi = 0°$ is presented in Figs. 3(b)–3(d). Furthermore, here each column shows a detailed analysis of selected conductance curves from Fig. 2(d).

whose tunneling processes to/from a molecule are modeled by the Hamiltonian

$$\hat{\mathcal{H}}_{\rm tun} = \sum_{qkl\sigma} t_l^q \hat{d}_{l\sigma}^\dagger \hat{a}_{k\sigma}^q + \text{H.c.}$$
$$= \sum_{qk\sigma} \sum_{a_N b_{N+1}} T^{\sigma q}_{a_{N+1} b_N} |a_{N+1}\rangle\langle b_N| \hat{a}_{k\sigma}^q + \text{H.c.}, \quad \text{(B2)}$$

with

$$T^{\sigma q}_{a_{N+1} b_N} = \sum_l t_l^q \langle a_{N+1}|\hat{d}_{l\sigma}^\dagger|b_N\rangle, \quad \text{(B3)}$$

where t_l^q is the tunneling matrix element, $\hat{d}_{l\sigma}^\dagger$ represents creation of an electron with spin σ in the molecular orbital l, and $\hat{a}_{k\sigma}^q$ denotes the annihilation operator for the qth electrode with k standing for an orbital quantum number. Note that the molecular state has been expanded in the basis of eigenvectors $|a_{N+1}\rangle$ and $|b_N\rangle$ of $\hat{\mathcal{H}}_{\rm SMM} = \sum_{n=N,N+1} \hat{\mathcal{H}}_{{\rm SMM},n}$. Next, we express the molecular eigenstates $|a_N\rangle$ and $|b_{N+1}\rangle$ with respect to the basis of angular momentum (spin) eigenstates. In principle, an arbitrary molecular state can be decomposed as $|\chi_n\rangle = \sum_{S_n M_n} \chi_{S_n M_n} |S_n M_n\rangle$. As a result, one obtains

$$T^{\sigma q}_{a_{N+1} b_N} = \sum_l \sum_{S_{N+1} M_{N+1}} \sum_{S_N M_N} t_l^q a^*_{S_{N+1} M_{N+1}} b_{S_N M_N}$$
$$\times \langle S_{N+1} M_{N+1}|\hat{d}_{l\sigma}^\dagger|S_N M_N\rangle. \quad \text{(B4)}$$

The key problem one encounters when analyzing the above equation is that the operator $\hat{d}_{l\sigma}^\dagger$ involves two degrees of freedom, namely, the orbital one (l) and the spin one (σ). Consequently, it may seem that in the next step we need

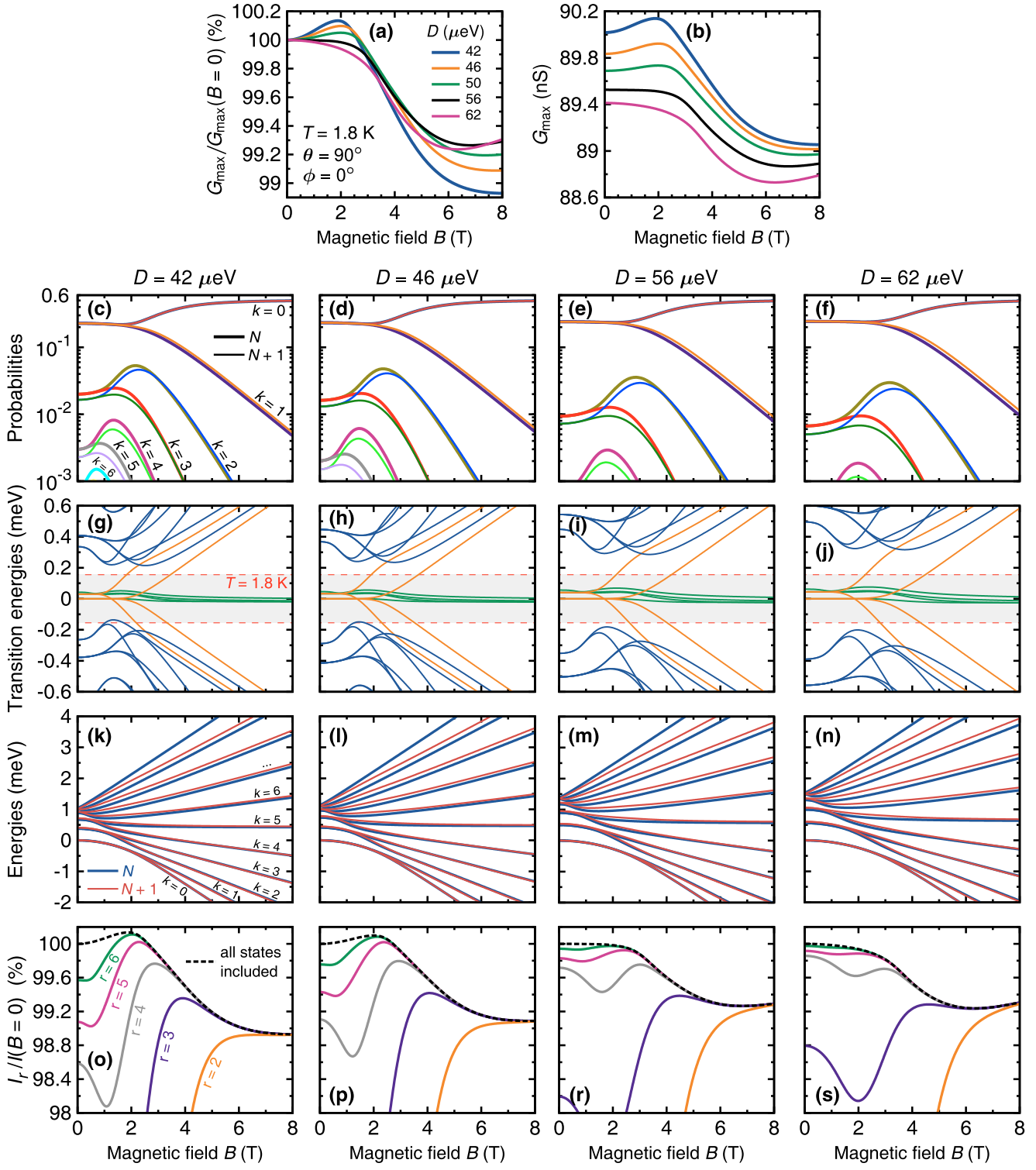

FIG. 16. (Color online) Evolution of the CP amplitude in the absence of transverse magnetic anisotropy ($E = 0$). This figure serves to illustrate the fact that even if the transverse magnetic anisotropy is absent, by making the uniaxial magnetic anisotropy parameter D smaller (keeping a fixed temperature), one can eventually also produce a maximum as for $E \neq 0$. However, this maximum occurs at a completely different (smaller) value of magnetic field. Moreover, the shape of $G_{\max}(B)$ remains invariant under rotation of the field in the hard plane; this is when the angle ϕ is varied. None of these are the case in the experiment under discussion. (a),(b) Dependence of $G_{\max}(B)$ on the value of the uniaxial magnetic anisotropy parameter $D \equiv D_N$ (and $D_{N+1} = 1.2D$) for an external magnetic field applied along the molecule's hard axis ($\theta = 90^\circ$ and $\phi = 0^\circ$). A detailed analysis of selected curves from (a),(b) is carried out in (c)–(s), with each column corresponding to the indicated value of D.

to calculate $\langle S_{N+1}M_{N+1}|\hat{d}^{\dagger}_{l\sigma}|S_N M_N\rangle$ explicitly. This complication, however, can be avoided by making use of the the Wigner-Eckart theorem [39], which basically allows for finding matrix elements of an operator with respect to angular momentum eigenstates,

$$\langle S_{N+1}M_{N+1}|\hat{d}^{\dagger}_{l\sigma}|S_N M_N\rangle = \langle S_N, M_N; \tfrac{1}{2},\sigma|S_{N+1}, M_{N+1}\rangle \times \langle S_{N+1}||\hat{d}^{\dagger}_{l}||S_N\rangle. \quad \text{(B5)}$$

The first factor of the right-hand side is a Clebsch-Gordan coefficient for adding spins S_N and $1/2$ to get S_{N+1}. This depends only on how the system is oriented with respect to the z axis. On the other hand, the second factor, the so-called *reduced matrix element*, remains independent of the spatial orientation, as it does not contain the magnetic quantum numbers M_N, M_{N+1}, or σ. Thus, we get

$$T^{\sigma q}_{a_{N+1}b_N} = \sum_{S_N S_{N+1}} \mathcal{T}^{\sigma}_{a_{N+1}b_N}\, \mathbb{T}^{q}_{S_{N+1}S_N}, \quad \text{(B6)}$$

with

$$\mathcal{T}^{\sigma}_{a_{N+1}b_N} = \sum_{M_N M_{N+1}} a^{*}_{S_{N+1}M_{N+1}} b_{S_N M_N} \times \langle S_N, M_N; \tfrac{1}{2},\sigma|S_{N+1}, M_{N+1}\rangle, \quad \text{(B7)}$$

and the term $\mathbb{T}^{q}_{S_{N+1}S_N} = \sum_l t^{q}_l \langle S_{N+1}||\hat{d}^{\dagger}_l||S_N\rangle$ regarded in calculations as a *single* free parameter to be adjusted for each electrode. Specifically, assuming a symmetric coupling between the molecule and two identical electrodes ($t^{L}_l = t^{R}_l$), the tunnel coupling takes the from $\Gamma_L = \Gamma_R = \Gamma/2$, where $\Gamma = 2\pi\rho|\mathbb{T}_{S_{N+1}S_N}|^2$ and ρ denotes the constant, spin-independent density of states in electrodes.

The stationary current I flowing through a molecule is calculated as $I = (I_L - I_R)/2$, where I_q (for $q = L, R$) stands for the current flowing from the qth electrode to the molecule,

$$I_q = \frac{e\Gamma}{2\hbar}\sum_{nn'}\sum_{a_n b_{n'}}(n'-n) f_q(\Delta\varepsilon_{b_{n'},a_n}) \sum_{\sigma\in q}\left|\mathcal{T}^{\sigma}_{b_{n'},a_n}\right|^2 \mathcal{P}_{a_n}. \quad \text{(B8)}$$

where $\Delta\varepsilon_{b,a} = \varepsilon_b - \varepsilon_a$, and $f_q(\omega) = \{1 + \exp[(\omega - \mu_q)/(k_B T)]\}^{-1}$ is the Fermi-Dirac function of the qth electrode, with T and $\mu_{L(R)} = \mu_0 \pm eV_b/2$ standing for temperature and the relevant electrochemical potential, respectively. The probabilities $\mathcal{P}_{a_n}$ of finding an SMM in a specific state $|a_n\rangle$ are then derived from a stationary master equation [16]. Finally, since SMMs are typically characterized by long spin coherence and spin relaxation times as a result of a weak spin-orbit and hyperfine coupling to the environment [2,40,41], we neglect relaxation of the spin states due to processes other than due to the electron tunneling.

In Fig. 3(d), and also in Figs. 13–16, we present the current $I_r = (I^r_L - I^r_R)/2$, which includes first r lowest-in-energy states in the spin multiplet of each charge state. We use this to show that many excited states in both charge state have to be taken into account in order to describe current correctly. We define I^r_q as

$$I^r_q = \frac{e\Gamma}{2\hbar}\sum_{nn'}\sum_{b_{n'}}\sum_{a_n}{}'^{r}(n'-n) f_q(\Delta\varepsilon_{b_{n'},a_n}) \sum_{\sigma\in q}\left|\mathcal{T}^{\sigma}_{b_{n'},a_n}\right|^2 \mathcal{P}_{a_n}, \quad \text{(B9)}$$

with $(\sum')^{r}_{a_n}$ denoting summation over states $|a_n\rangle$ in the charge state n that is limited only to first r states of lowest energy.

4. Signatures of the transverse anisotropy parameter E without the Berry-phase oscillations

In Figs. 2(a) and 3 we discuss the initial increase of the current with magnetic field followed by a decrease. The key insight of our calculations using the method described in the previous section (Appendix B3) is that the mechanism for this effect is significantly enhanced and modified for $E \neq 0$, giving rise to the characteristic $G_{\max}$ curves shown in Fig. 2. Since this is at the basis of our scheme of detection, it deserves a further comment. In particular, the relation to the Berry-phase oscillations which underlay most of the previously used techniques for determining the parameter E.

(i) Upon increase of E the minima of the transition-energy curves are shifted to higher field values and the value achieved at the minimum is lowered; cf. Fig. 3(c) with Figs. 13(e)–13(h). For a fixed temperature, this leads to a more pronounced maximum conductance attained at a higher field value.

(ii) Generally, the transition energies in Fig. 3(c) show sharp features (i.e., oscillations below $B = 2$ T) due to Berry-phase interference on which several techniques for extracting E rely, by analyzing the field dependence of the tunnel splitting between two selected states [1,12,14,19]. However, the detection of such behavior in the conductance requires very specific low-temperature conditions. This is in contrast to the present experimental conditions where these Berry-phase features are averaged out when taking into account multiple accessible states. This leaves only the large-scale, collective variations of the transition-energy spectrum caused by E, which, as we have shown, suffice for estimation of E. In Fig. 3(d) we illustrate the importance of taking into account many excited states for both charge states to describe current correctly.

(iii) Finally, Fig. 2(c) shows the relative CP amplitude for increasing E/D. A qualitative distinction from the $E \ll D$ limit is the appearance of an additional shoulder close to $B = 6$ T. It is tempting to see such a shoulder in the sample A curve of Fig. 2(a), although the sample B curve exhibits features of similar size where it should theoretically be smooth. In summary, the calculations certainly show that a sizable E term leads to fingerprints in the linear conductance as clear as those for the D term, even for relatively high temperatures.

[1] D. Gatteschi, R. Sessoli, and J. Villain, *Molecular Nanomagnets* (Oxford University Press, New York, 2006).
[2] L. Bogani and W. Wernsdorfer, Nat. Mater. **7**, 179 (2008).
[3] J. Grose, E. Tam, C. Timm, M. Scheloske, B. Ulgut, J. Parks, H. Abruña, W. Harneit, and D. Ralph, Nat. Mater. **7**, 884 (2008).

[4] J. Parks, A. Champagne, T. Costi, W. Shum, A. Pasupathy, E. Neuscamman, S. Flores-Torres, P. Cornaglia, A. Aligia, C. Balseiro, G.-L. Chan, H. Abruña, and D. Ralph, Science **328**, 1370 (2010).
[5] A. Zyazin, J. van den Berg, E. Osorio, H. van der Zant, N. Konstantinidis, M. Leijnse, M. Wegewijs, F. May, W. Hofstetter, C. Danieli, and A. Cornia, Nano Lett. **10**, 3307 (2010).
[6] M. Urdampilleta, S. Klyatskaya, J.-P. Cleuziou, M. Ruben, and W. Wernsdorfer, Nat. Mater. **10**, 502 (2011).
[7] R. Vincent, S. Klyatskaya, M. Ruben, W. Wernsdorfer, and F. Balestro, Nature (London) **488**, 357 (2012).
[8] M. Mannini, F. Pineider, P. Sainctavit, C. Danieli, E. Otero, C. Sciancalepore, A. Talarico, M. Arrio, A. Cornia, D. Gatteschi, and R. Sessoli, Nat. Mater. **8**, 194 (2009).
[9] M. N. Leuenberger and D. Loss, Nature (Lodnon) **410**, 789 (2001).
[10] F. Troiani and M. Affronte, Chem. Soc. Rev. **40**, 3119 (2011).
[11] S. Thiele, F. Balestro, R. Ballou, S. Klyatskaya, M. Ruben, and W. Wernsdorfer, Science **344**, 1135 (2014).
[12] D. Gatteschi and R. Sessoli, Angew. Chem. Int. Ed. **42**, 268 (2003).
[13] M. Misiorny and J. Barnaś, Phys. Rev. Lett. **111**, 046603 (2013).
[14] W. Wernsdorfer and R. Sessoli, Science **284**, 133 (1999).
[15] C. Romeike, M. R. Wegewijs, W. Hofstetter, and H. Schoeller, Phys. Rev. Lett. **96**, 196601 (2006).
[16] C. Romeike, M. R. Wegewijs, and H. Schoeller, Phys. Rev. Lett. **96**, 196805 (2006).
[17] M. N. Leuenberger and E. R. Mucciolo, Phys. Rev. Lett. **97**, 126601 (2006).
[18] G. González and M. N. Leuenberger, Phys. Rev. Lett. **98**, 256804 (2007).
[19] E. Burzurí, F. Luis, O. Montero, B. Barbara, R. Ballou, and S. Maegawa, Phys. Rev. Lett. **111**, 057201 (2013).
[20] S. Accorsi, A. L. Barra, A. Caneschi, G. Chastanet, A. Cornia, A. C. Fabretti, D. Gatteschi, C. Mortalo, E. Olivieri, F. Parenti, P. Rosa, R. Sessoli, L. Sorace, W. Wernsdorfer, and L. Zobbi, J. Am. Chem. Soc. **128**, 4742 (2006).
[21] M. Mannini, F. Pineider, C. Danieli, F. Totti, L. Sorace, P. Sainctavit, M.-A. Arrio, E. Otero, L. Joly, J. C. Cezar, A. Cornia, and R. Sessoli, Nature (London) **468**, 417 (2010).
[22] S. Carretta, P. Santini, G. Amoretti, T. Guidi, R. Caciuffo, A. Candini, A. Cornia, D. Gatteschi, M. Plazanet, and J. A. Stride, Phys. Rev. B **70**, 214403 (2004).
[23] D. Ferry, S. Goodnick, and J. Bird, *Transport in Nanostructures* (Cambridge University Press, Cambridge, UK, 2009).
[24] E. Burzurí, A. S. Zyazin, A. Cornia, and H. S. J. van der Zant, Phys. Rev. Lett. **109**, 147203 (2012).
[25] A. Zyazin, H. van der Zant, M. Wegewijs, and A. Cornia, Synth. Met. **161**, 591 (2011).
[26] R. Hanson, L. Kouwenhoven, J. Petta, S. Tarucha, and L. Vandersypen, Rev. Mod. Phys. **79**, 1217 (2007).
[27] L. Gregoli, C. Danieli, A.-L. Barra, P. Neugebauer, G. Pellegrino, G. Poneti, R. Sessoli, and A. Cornia, Chem. Eur. J. **15**, 6456 (2009).
[28] C. Timm and F. Elste, Phys. Rev. B **73**, 235304 (2006).
[29] M. Misiorny, I. Weymann, and J. Barnaś, Phys. Rev. B **79**, 224420 (2009).
[30] M. Leijnse and M. R. Wegewijs, Phys. Rev. B **78**, 235424 (2008).
[31] R. Bulla, T. Costi, and T. Pruschke, Rev. Mod. Phys. **80**, 395 (2008).
[32] A. I. Tóth, C. P. Moca, Ö. Legeza, and G. Zaránd, Phys. Rev. B **78**, 245109 (2008).
[33] O. Legeza, C. Moca, A. Tóth, I. Weymann, and G. Zaránd, Manual for the flexible DM-NRG code, arXiv:0809.3143, the open access Budapest code is available at http://www.phy.bme.hu/∼dmnrg/.
[34] A. Wilson, J. Lawrence, E.-C. Yang, M. Nakano, D. N. Hendrickson, and S. Hill, Phys. Rev. B **74**, 140403 (2006).
[35] F. May, M. Wegewijs, and W. Hofstetter, Beilstein J. Nanotechnol. **2**, 693 (2011).
[36] E. Burzuri, Y. Yamamoto, M. Warnock, X. Zhong, K. Park, A. Cornia, and H. van der Zant, Nano Lett. **14**, 3191 (2014).
[37] O. Kahn, *Molecular Magnetism* (VCH, New York, 1993).
[38] R. Boča, *Theoretical Foundations of Molecular Magnetism*, Current Methods in Inorganic Chemistry (Elsevier, Lousanne, Switzerland, 1999), Vol. 1.
[39] A. Messiah, *Quantum Mechanics* (Dover, New York, 1999).
[40] A. Ardavan, O. Rival, J. J. L. Morton, S. J. Blundell, A. M. Tyryshkin, G. A. Timco, and R. E. P. Winpenny, Phys. Rev. Lett. **98**, 057201 (2007).
[41] S. Bertaina, S. Gambarelli, T. Mitra, B. Tsukerblat, A. Müller, and B. Barbara, Nature (London) **453**, 203 (2008).